Geophysical Research Letters

RESEARCH LETTER
10.1029/2025GL115137

Inferring Tectonic Plate Rotations From InSAR Time Series

Yuan-Kai Liu[1], Zhang Yunjun[1,2,3], and Mark Simons[1]

[1]Seismological Laboratory, Division of Geological and Planetary Sciences, California Institute of Technology, Pasadena, CA, USA, [2]Now at National Key Laboratory of Microwave Imaging, Aerospace Information Research Institute, Chinese Academy of Sciences, Beijing, China, [3]Now at School of Electronic, Electrical and Communication Engineering, University of Chinese Academy of Sciences, Beijing, China

Key Points:

- We demonstrate that large-scale Interferometric Synthetic Aperture Radar (InSAR) line-of-sight velocity gradient can be used to infer the angular velocity vector of the Arabian plate
- Accounting for atmospheric path delays enables matching the GNSS-derived angular velocity vector with mm/year uncertainty
- The current lack of sensitivity to north-south motions from InSAR data accounts for most of the uncertainty in the determination of plate rotations

Supporting Information:

Supporting Information may be found in the online version of this article.

Correspondence to:

Y.-K. Liu,
ykliu@caltech.edu

Citation:

Liu, Y.-K., Yunjun, Z., & Simons, M. (2025). Inferring tectonic plate rotations from InSAR time series. *Geophysical Research Letters*, *52*, e2025GL115137. https://doi.org/10.1029/2025GL115137

Received 3 FEB 2025
Accepted 2 JUN 2025

Author Contributions:

Conceptualization: Yuan-Kai Liu, Zhang Yunjun, Mark Simons
Data curation: Yuan-Kai Liu
Formal analysis: Yuan-Kai Liu
Funding acquisition: Mark Simons
Methodology: Yuan-Kai Liu, Zhang Yunjun, Mark Simons
Supervision: Mark Simons
Visualization: Yuan-Kai Liu
Writing – original draft: Yuan-Kai Liu
Writing – review & editing: Yuan-Kai Liu, Zhang Yunjun, Mark Simons

Abstract Interferometric Synthetic Aperture Radar (InSAR) provides constraints on lithospheric kinematics at high spatial resolution. Interpreting InSAR-derived deformation maps at continental scales is challenged by long-wavelength correlated noise and the inherent limitation of measuring relative displacements within the data footprint. We address these issues by applying corrections to InSAR time series to estimate ground velocity fields with millimeter-per-year precision over hundreds of kilometers. We use these velocity fields to determine the angular velocity of the local tectonic plate, assuming negligible long-wavelength vertical and intra-plate deformation. The uncertainty of the angular velocity is primarily influenced by observational errors and the limited imaging geometries available. Using the Arabian plate as an example, this work demonstrates the potential to improve plate motion models and evaluate intra-plate deformation in regions with sparse ground-based instrumentation.

Plain Language Summary Quantifying how tectonic plates move is key to understanding how Earth's surface deforms over time. Plate motions have traditionally been estimated using global navigation satellite system (GNSS) observations. However, GNSS stations are often unevenly distributed, especially away from active plate boundaries, making it harder to precisely determine broad-scale plate motions. Interferometric Synthetic Aperture Radar (InSAR), a satellite-based radar technique, offers widespread spatial coverage but measures only relative displacements along the satellite's line-of-sight, and it is often contaminated by long-wavelength noise. Here, we explore using InSAR to constrain the rotation field of the rigid Arabian plate. We developed a method to correct for long-wavelength contributions of non-tectonic sources and extract absolute plate rotation from spatial gradients in InSAR-measured relative velocities. By assuming negligible large-scale vertical motion and horizontal intra-plate deformation, InSAR velocity alone can determine a plate's Euler pole in the International Terrestrial Reference Frame (ITRF14). This approach demonstrates the broader potential for combining satellite and ground data to better understand tectonic plate kinematics and eventually dynamics of lithospheric processes.

1. Introduction

Geodetic observations of the partitioning of deformation across plate boundaries are crucial for understanding lithospheric dynamics. Key issues include the consistency of geodetic and geologic deformation rates, the appropriateness of the rigid plate approximation, and the rate of seismogenic strain accumulation (e.g., Argus & Gordon, 1996; Loveless & Meade, 2010; McCaffrey, 2005; Tong et al., 2014). Global models of rigid plate motion provide the context for assessing deformation partitioning (e.g., Argus et al., 2011; DeMets et al., 2010; Kreemer et al., 2014). Traditionally, these plate motion models are predicted from plate angular velocity vectors derived using global navigation satellite system (GNSS) observations and are limited by instrumental coverage, especially in plate interiors. However, large-scale $\left(10^2–10^3 \text{ km}\right)$ surface motion can now be mapped with great precision using Interferometric Synthetic Aperture Radar (InSAR) (e.g., Lemrabet et al., 2023; Ou et al., 2022; Stephenson et al., 2022; Weiss et al., 2020; Xu et al., 2021), thereby providing useful constraints in sparsely instrumented regions.

Despite the near-complete spatial continuity of InSAR-derived velocity fields, their long-wavelength information is often underutilized (Chaussard et al., 2016; Parizzi et al., 2021). For example, when studying seismic processes along active fault zones, an empirical low-order polynomial velocity field is typically removed to alleviate long-wavelength orbital or atmospheric effects (e.g., Biggs et al., 2007; Cavalié et al., 2008; Massonnet et al., 1993; Pritchard & Simons, 2006; Simons et al., 2002; Ryder et al., 2007). For investigating long-wavelength

10.1029/2025GL115137

(10^2–10^3 km) distributed strain, InSAR velocity fields are often aligned to deformation models interpolated from GNSS networks (e.g., Fialko, 2006; Jolivet et al., 2015; Lemrabet et al., 2023; Neely et al., 2020; Tong et al., 2013), which simultaneously mosaics individually referenced velocity fields to an internally consistent reference frame. When such a network is unavailable, unassisted use of InSAR-derived velocities over continental scales requires accounting for spatially correlated signals of confounding origins (Fattahi & Amelung, 2014; Chaussard, Bürgmann, Fattahi, Johnson, et al., 2015, Chaussard, Bürgmann, Fattahi, Nadeau, et al., 2015), including spatiotemporal variations of troposphere (Emardson et al., 2003; Onn & Zebker, 2006; Tarayre & Massonnet, 1996), ionosphere (Gomba et al., 2016; Gray et al., 2000; Meyer, 2010) and the lithospheric responses to tides and surface mass loading (Biggs et al., 2007; DiCaprio & Simons, 2008; Xu & Sandwell, 2020).

Recent large-area studies demonstrate the potential to constrain lateral plate motions using InSAR observations. Lazecký et al. (2023) applied burst-overlap interferometry (Grandin et al., 2016; Li et al., 2021) over regions including the Alpine-Himalayan Belt, yielding averaged horizontal velocities that agree with the ITRF2014 plate motion model, with median 2-sigma errors of 4 mm/yr northwards and 23 mm/yr eastwards. When inferring interseismic fault coupling of the East Anatolian and North Anatolian Faults, Bletery et al. (2020) combined InSAR and GNSS observations to estimate local Euler vectors of Arabia and Anatolia relative to stable Eurasia. Using exclusively InSAR-derived relative LOS velocities, Stephenson et al. (2022) showed that plate motions manifest themselves as velocity gradients (see also Bähr, 2013; Bähr et al., 2012), consistent with the ITRF2014 plate motion model (Altamimi et al., 2017) within 0.2 mm/yr/100 km in Makran, Arabia, and Australia. Later, Lemrabet et al. (2023) showed that large-scale velocity ramps can be used to retrieve the plate motion in the ITRF reference frame and quantify their consistency against GNSS derived plate motion. Here, we address the inverse problem and use long-wavelength InSAR velocity fields from multiple orbital tracks to determine the Euler vector for the Arabian plate.

2. Methods

2.1. Interferograms Processing and Velocity Corrections

We process nine tracks of Sentinel-1A Interferometric Wide Swath mode Level-1 SLCs (single-look complex images, each covering 250 × 250 km; Figure 1) spanning 2014–2023 (∼250 epochs). SLCs from the same track are coregistered using precise orbits and the 1-arcsecond SRTM v3.0 elevation model (Farr et al., 2007), all relative to the WGS84 ellipsoid. For finer azimuthal coregistration, We apply a network-based enhanced spectral diversity approach (Fattahi et al., 2017). We construct a fully connected, small-baseline interferometric network (Berardino et al., 2002) by pairing each acquisition with all the neighbors within 2 months and with the acquisitions that were acquired 4 months apart. Approximately 900 interferograms per track are multilooked to ∼500-m ground-pixel resolution, filtered using a power-spectrum adaptive filter with an exponent of 0.5 (Goldstein & Werner, 1998), and unwrapped using a minimum cost-flow algorithm (Chen & Zebker, 2002).

We estimate deformation time series using a least-squares inversion weighted by the inverse of phase variance (Guarnieri & Tebaldini, 2008; Tough et al., 1995) while minimizing the implied velocities in all time intervals (Berardino et al., 2002; Yunjun et al., 2019). In the time-series domain, we apply corrections to account for stratified tropospheric delays (Jolivet et al., 2011, 2014) based on the ECMWF ReAnalysis model (ERA5) (Hersbach et al., 2020), ionospheric effects using a range split-spectrum method (Liang et al., 2019), solid earth tides (SET) (Milbert, 2018; Yunjun et al., 2022), the elastic response to ocean tidal loading (OTL) (Martens et al., 2019), phase closure bias (Zheng et al., 2022), and residual baseline-related topographic phases (Fattahi & Amelung, 2013). We fit pixel-wise time series to a temporal function consisting of secular velocity plus annual and semi-annual sinusoids (Text S2 in Supporting Information S1; Hetland et al., 2012). Low-quality pixels with temporal coherence <0.9 are masked (Yunjun et al., 2019), as are pixels where the cumulative closure phase exceeds three times the standard deviation (Zheng et al., 2022). We exclude clearly deforming regions near (within 60 km) the Dead Sea Transform Fault to reduce the effects of seismic cycle and rifting processes (Castro-Perdomo et al., 2021; Klinger et al., 1999; Li et al., 2021; Reilinger et al., 2006). For simplicity, we do not model the relative motion of the Sinai subplate to Arabia (Mahmoud et al., 2005). The final velocity field is geocoded and downsampled to a 2.5 km posting.

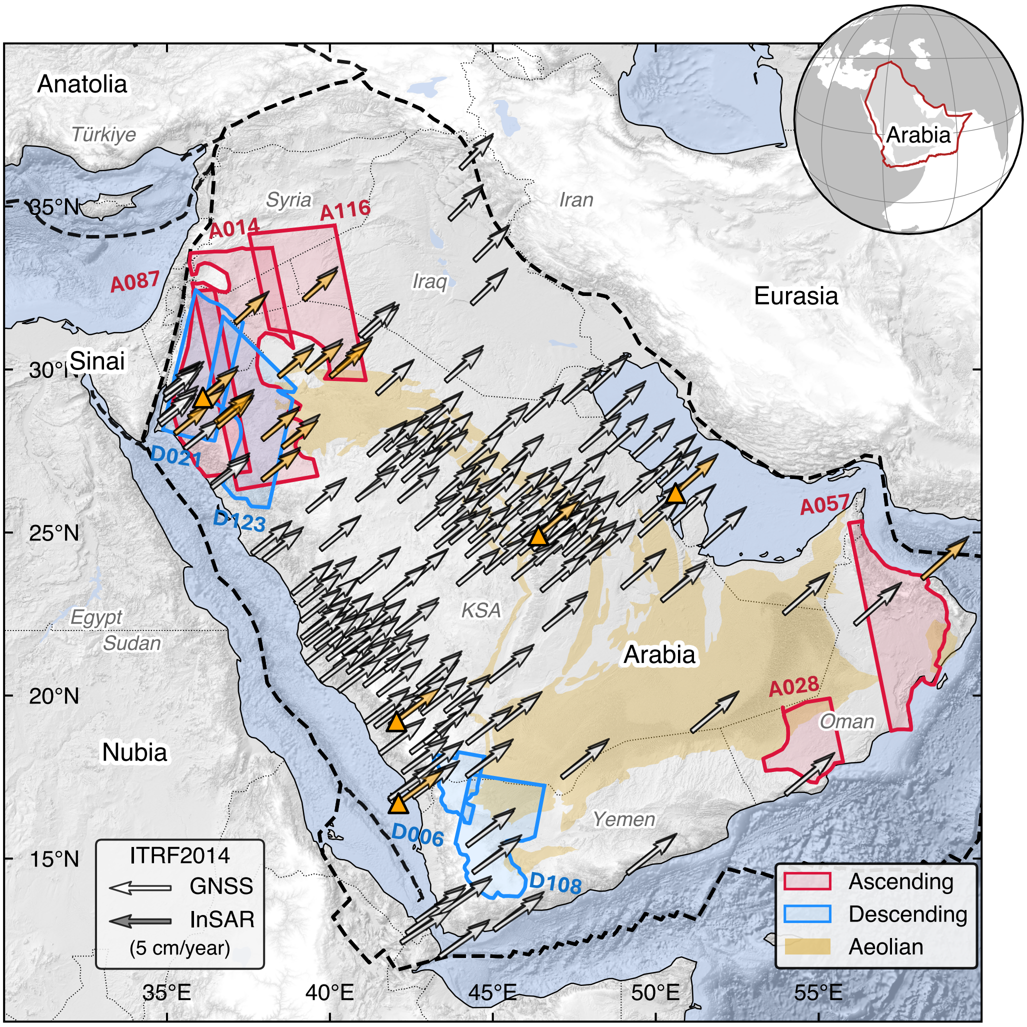

Figure 1. Arabian plate velocities predicted by global navigation satellite system (GNSS)-derived (Viltres et al., 2022, shown as white arrows. The orange arrows are stations used for our geometry tests in Section 3.3. Text S1 in Supporting Information S1) and our Interferometric Synthetic Aperture Radar (InSAR)-derived (dark arrows) Euler vector in International Terrestrial Reference Frame 2014. The orange triangles indicate the GNSS stations used to derive the Arabian Euler vector by Altamimi et al. (2017). Brown shading marks dune regions that decorrelate interferograms. The red (ascending) and blue (descending) rectangles indicate the extent of the InSAR measurements used in this study. Plate boundaries are compiled from Argus et al. (2011), Bird (2003), and Viltres et al. (2022).

2.2. InSAR-Based Euler Vector Estimation

Leveraging spatially relative InSAR measurements to constrain the absolute rotation of tectonic plates in a global reference frame forms a central tenet of this work. This apparent contradiction is resolved by exploiting the intrinsic geometric properties of radar imaging. The systematic variation in the satellite's look angle across the imaging swath induces a predictable quasi-range-dependent LOS velocity gradient that, under the assumption of rigid plate motion and negligible long-wavelength vertical motion, becomes proportional to the absolute angular velocity vector (Bähr et al., 2012; Lemrabet et al., 2023; Stephenson et al., 2022).

InSAR LOS measurements and the derived velocities are with respect to the orbital positions of Sentinel-1 in no-net-rotation (NNR) ITRF2014 (Peter, 2021). Assuming the large-scale vertical motion can be ignored, we write the ground velocity in ITRF projected along the satellite LOS as a sum of the following components:

$$\mathbf{d} = \mathbf{d}_{\mathrm{B}} + \mathbf{d}_{\varepsilon}, \tag{1}$$

10.1029/2025GL115137

where $\mathbf{d}_B$ is the linear velocity due to plate rotation, and $\mathbf{d}_\varepsilon$ is the velocity due to internal deformation relative to $\mathbf{d}_B$, including elastic strain of plate boundaries and distributed intra-plate strain (e.g., Meade & Loveless, 2009). When $\mathbf{d}_\varepsilon$ negligible, the ground velocity can be modeled as an Euler vector (i.e., angular velocity vector), $\mathbf{m} = [\mathrm{m_x}, \mathrm{m_y}, \mathrm{m_z}]^\intercal$ (rad/yr) (Cox & Hart, 1986; McKenzie & Parker, 1967; Morgan, 1968). The Euler vector maps to the pixel-wise LOS velocity $\mathbf{d}$ for P number of pixels via a linear transformation matrix, $\mathbf{G}$, which is fully determined by the coordinates and LOS angles of each InSAR pixel (Text S3 in Supporting Information S1) such that

$$\mathbf{d} = \mathbf{G}\ \mathbf{m} \tag{2}$$

where $\mathbf{d}$, $\mathbf{G}$, and $\mathbf{m}$ have dimensions $[P \times 1]$, $[P \times 3]$, and $[3 \times 1]$, respectively. The InSAR displacement and velocity is usually described relative to a reference pixel (e.g., Massonnet & Feigl, 1998), $\mathbf{r}^*$, where the derived displacement and velocity are assumed to be zero. To align the linear model with our relative measurements, we reference $\mathbf{G}$ to the common reference pixel in each track by subtracting the row corresponding to the reference pixel, $\mathbf{G}^* = \mathbf{G} - \mathbf{G}_{\mathbf{r}^*}$. We then can formulate a linear problem with the measured relative velocity, $\mathbf{d}^*$

$$\mathbf{d}^* = \mathbf{G}^*\ \mathbf{m} \tag{3}$$

Consequently, the local velocity gradient tensor observed in each relative InSAR track $\mathbf{d}^*$, encodes information about the absolute Euler vector $\mathbf{m}$ in ITRF2014, and the mapping relation is defined by the sensing matrix $\mathbf{G}$. The maximum likelihood solution is given by

$$\hat{\mathbf{m}} = \mathbf{C}_{\hat{\mathrm{m}}} \mathbf{G}^{*\intercal} \mathbf{C}_{\mathrm{d}^{-1}} \mathbf{d}^* \tag{4}$$

with covariance

$$\mathbf{C}_{\hat{\mathrm{m}}} = \left(\mathbf{G}^{*\intercal} \mathbf{C}_{\mathrm{d}^{-1}} \mathbf{G}^*\right)^{-1} \tag{5}$$

where the estimate of the Euler vector, $\hat{\mathbf{m}}$, and its model covariance, $\mathbf{C}_{\hat{\mathrm{m}}}$, depends on the observational covariance $\mathbf{C}_\mathrm{d}$ which is dictated by measurement uncertainty.

2.3. Covariance Model at a Single Reference

Residual noise remains in interferometric phase measurements even after applying deterministic corrections, introducing uncertainties in ground velocity estimates. We assume there is no bias in the long-wavelength velocity gradient, and following previous studies (e.g., Agram & Simons, 2015), we model the short-to intermediate-wavelength (<100 km) phase noise as stochastic variables in the velocity fields

$$\mathbf{d}^* = \mathbf{G}^*\ \mathbf{m} + \mathbf{d}_{\mathrm{resid}}, \tag{6}$$

where the stochastic component

$$\mathbf{d}_{\mathrm{resid}} = \mathbf{d}_{\mathrm{corr}} + \mathbf{d}_{\mathrm{uncorr}} + \mathbf{d}_{\mathrm{ref}}. \tag{7}$$

The first two terms represent the deviations of pixel-wise velocities from pure ground displacements in imperfect measurements. $\mathbf{d}_{\mathrm{corr}}$ represents apparent velocity contribution due to spatially correlated residual noise (uncertainties in the atmospheric structures), and $\mathbf{d}_{\mathrm{uncorr}}$ represents the velocity noise due to the phase contribution from spatio-temporally uncorrelated noise sources (e.g., decorrelation noise, uncorrelated troposphere in time, phase unwrapping errors). It is reasonable to assume these sources of noise to be zero mean random variables and describe the observational covariance matrix as

$$\mathbf{C}_\mathrm{d} = \mathbf{C}_{\mathrm{d_s}} + \mathbf{C}_{\mathrm{d_t}}, \tag{8}$$

where $\mathbf{C}_{\mathrm{d_s}}$ accounts for the stationary and isotropic intermediate-wavelength spatial correlation of $\mathbf{d}_{\mathrm{corr}}$ (Hanssen, 2001). We remove a quadratic ramp from velocity before computing $\mathbf{C}_{\mathrm{d_s}}$ using a distance-dependent exponential function fitted to the sampled variogram for data point pairs within 300 km (Jónsson et al., 2002; Lohman & Simons, 2005; Simons et al., 2002). The characteristic length scales of the modeled covariance are 50–100 km. $\mathbf{C}_{\mathrm{d_t}}$ accounts for $\mathbf{d}_{\mathrm{uncorr}}$ and is a diagonal matrix populated with the variances of the pixel-wise velocity estimates determined by the functional-fit residuals assuming uniform Gaussian errors at all epochs (Fattahi & Amelung, 2015). The median of diagonals in $\mathbf{C}_{\mathrm{d_t}}$ and $\mathbf{C}_{\mathrm{d_s}}$ are of comparable magnitude, ranging from 0.4 to 0.8 mm/yr (Text S4.2 in Supporting Information S1).

2.4. Posterior From Ensemble References

Our velocities, observational errors, and the linear operator $\mathbf{G}^*$ are all described relative to a set of reference pixels (Equation 6). While guidelines exist for selecting such candidate pixels (Yunjun et al., 2019; Zhang et al., 2024), any real or apparent displacement (e.g., from atmospheric path delays) of the reference pixel, $\mathbf{d}_{\mathrm{ref}}$, will be redistributed to all the other pixels. To account for this limitation, we consider multiple realizations of the velocity field using different reference points. Specifically, we conduct 1,000 realizations of the Euler vector inversion (Equations 4 and 5), where each is based on velocity fields using randomly picked reference points for each track (Figure S4 in Supporting Information S1). We restrict the choice of reference such that it lies below an elevation of 1500 m and must be at least 25 km from masked areas). The measurement error, $\mathbf{C}_{\mathrm{d_t}}$, in each realization updates with the chosen reference, while $\mathbf{C}_{\mathrm{d_s}}$ remains unchanged due to the stationarity assumption of the deramped noise structure. These realizations yield an ensemble of Euler vectors (Section 3.2), from which we introduce and derive a mismodeling covariance matrix, $\mathbf{C}_{\mathrm{p}}$, to quantify the ensemble posterior. We estimate $\mathbf{C}_{\mathrm{p}}$ using the second moment of the ensemble predictions over all realizations (Duputel et al., 2012; Vasyura-Bathke et al., 2021):

$$(\mathbf{C}_{\mathrm{p}})^{ij} = \frac{1}{\mathrm{L}} \sum_{k=1}^{\mathrm{L}} \left(\mathbf{d}^{i}(\hat{\mathbf{m}}_k) - \bar{\mathbf{d}}^{i} \right) \left(\mathbf{d}^{j}(\hat{\mathbf{m}}_k) - \bar{\mathbf{d}}^{j} \right) \tag{9}$$

where i, j denote the rows and columns in the data covariance matrix; the total number of realizations, $\mathrm{L} = 1000$; $\mathbf{d}^{i}(\hat{\mathbf{m}}_k)$ represents the predicted data at pixel i with the kth realized Euler vector, corresponding to a reference point at $\mathbf{r}_k$. The term $\bar{\mathbf{d}}^{i} = \frac{1}{\mathrm{L}}\sum_{k=1}^{\mathrm{L}} \mathbf{d}_k^{i}(\hat{\mathbf{m}}_k)$ is the population mean of predictions at pixel i. We append this epistemic covariance to the total noise covariance matrix as $\mathbf{C}_{\chi} = \mathbf{C}_{\mathrm{d}} + \mathbf{C}_{\mathrm{p}}$ and invert for the posterior and uncertainty of the Euler vector using Equations 4 and 5, with $\mathbf{C}_{\chi}$ replacing $\mathbf{C}_{\mathrm{d}}$.

3. Results and Discussions

3.1. The Long-Wavelength Velocity Field

We demonstrate the process of inferring the long-wavelength velocity field using ascending (dusk) track A087 in northwest Arabia (Figure 2). The time series of ionospheric delay in dusk tracks contributes to secular apparent velocity with a gradient of ∼0.8 mm/yr/100 km. Due to solar cycles, the apparent velocity depends on the time span, and the gradient increases to ∼2.0 when fitted to data before January 2022. The ionospheric correction reduces ramp magnitudes and spatial standard deviation for all epochs (Figures 2i–2k).

The tropospheric model reduces temporal fluctuations, lowering median post-fit residuals by 10.1 mm for northwest Arabia, 6.1 mm for Oman, and 5.1 mm for Yemen tracks. The apparent velocity gradient predicted from ERA5 is minimal, at 0.1 mm/yr/100 km, similar to a kriging-interpolated method (Cao et al., 2021) and the GACOS (Yu et al., 2017) model. The largest tidal constituents, M2 and O1, have aliased periods of 64.1 and 77.7 days, respectively, when sampled every 12 days (Xu & Sandwell, 2020), so SET and OTL have minimal impact on decadal timescales. Phase closure biases and topographic residuals are localized and do not produce a velocity gradient greater than 0.1 mm/yr/100 km. After all corrections, we account for 70% of the ramps at the epoch level (Text S2.2 and Figure S1 in Supporting Information S1), leaving the final time series with standard deviations of 1.6–3 cm. The standard deviations of velocity estimates relative to the reference points are 0.4–0.8 mm/yr (Figures 2i and 3b) in the far field.

10.1029/2025GL115137

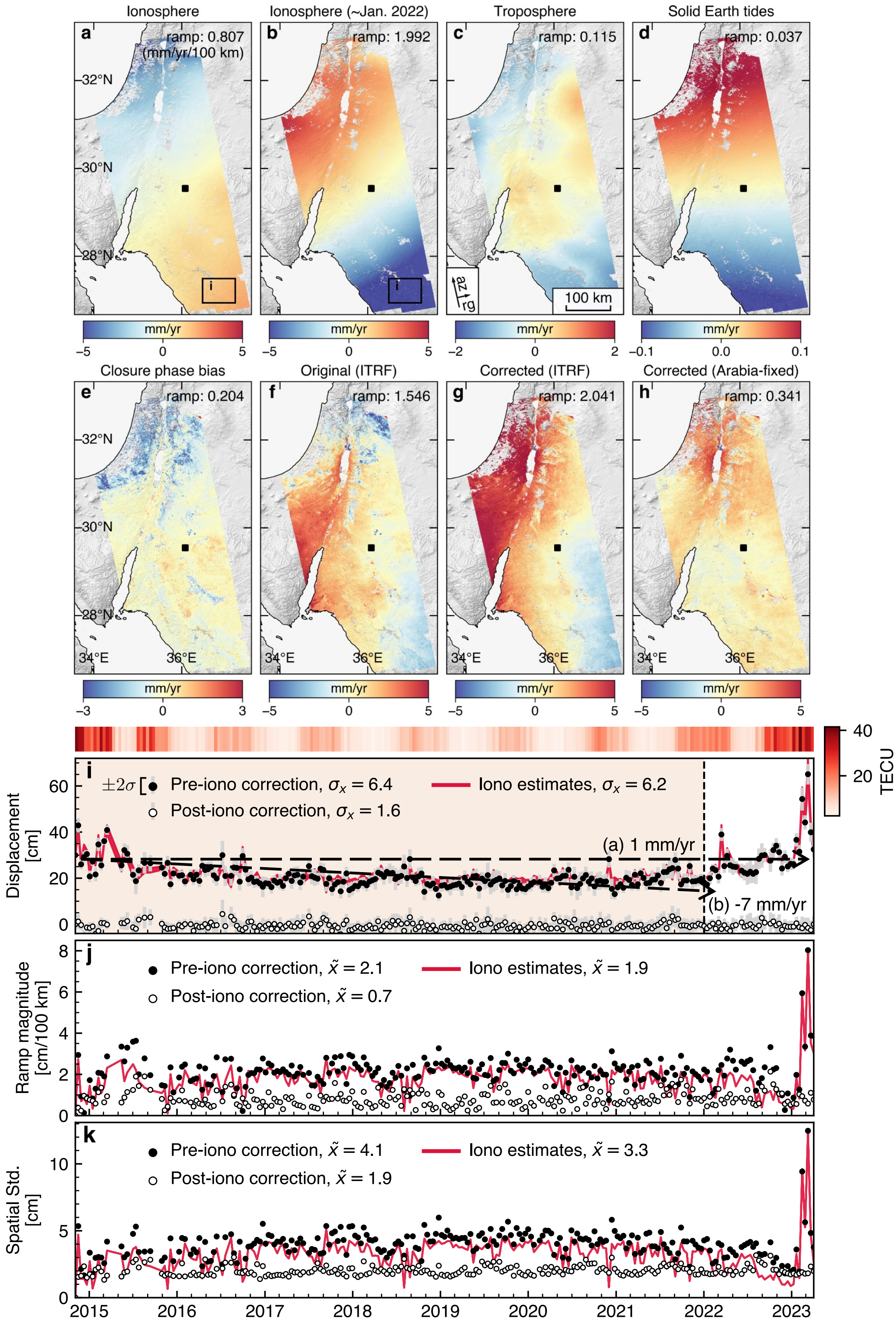

Figure 2.

Quasi-range-dependent velocity gradients of $\sim$2.1 mm/yr/100 km are present in multiple velocity tracks (Figures S2 and S10 in Supporting Information S1). A joint inversion of nine InSAR tracks arrives at an ITRF2014 Euler vector $\hat{\mathbf{m}} = [0.358, \ -0.055, 0.418]$ °/Ma. This predicts the same $\sim$2.1 mm/yr/100 km velocity gradient and horizontal velocities of 38–54 mm/yr across the Arabian plate (Figure 3c). Subtracting the prediction from the angular velocity of the plate, the residual velocity fields of ±2 mm/yr represent motion relative to the Arabian reference frame, which agree with horizontal GNSS data (Viltres et al., 2022) (Figures S11–S13 in Supporting Information S1). The largest discrepancies occur near the Dead Sea (4–5 mm/yr of lithospheric rebound), the Wadi Sirhan Basin near GNSS site JW03 (Figure 3d), and potential ionospheric correction artifacts near site TB06.

3.2. The Inferred Euler Vector

Several Euler vectors exist for the Arabian plate, including MORVEL56-NNR (Argus et al., 2011), GSRM v2.1 (Kreemer et al., 2014), the ITRF2014 plate model (Altamimi et al., 2017), and a recent GNSS-derived vector (Viltres et al., 2022). The rigid block approximation is appropriate in Arabia, and the Arabian vector of Altamimi et al. (2017) aligns well with Le Pichon and Kreemer (2010) and Viltres et al. (2022). Therefore, we use Altamimi et al. (2017) as the benchmark for comparisons (Figure 4).

The vector derived from the single realization of the velocities shown in Figure 3a lies between the MORVEL and Altamimi et al. (2017) ("x" marker in Figures 4a–4c). For 1,000 random reference points, the Euler vector realizations are distributed within 13.7° in latitude, 27.9° in longitude, and 0.1 °/Ma in rotation rate. Significant trade-offs occur along N60°E in geographic and latitudinal-rate spaces. The posterior Euler vector $\hat{\mathbf{m}} = [0.353, \ -0.049, 0.421]$ °/Ma is 182.7 km from the pole of Altamimi et al. (2017), with a 0.037°/Ma faster rotation rate. Our 2-sigma error bound overlaps with Altamimi et al. (2017). The mean differences in horizontal velocities are 1.015 mm/yr (east) and 3.269 mm/yr (north), indicating less constraint on north-south motion. Euler vector parameters and covariances are tabulated in Table S1 in Supporting Information S1. Our inversion does not account for uncertainty in the long-wavelength velocity gradient. Following the approach in Lemrabet et al. (2023) we empirically estimate the uncertainty of the long-wavelength velocity to be approximately $0.001-0.004$ mm/yr/km and can accumulate to $1-3$ mm/yr across the track (Text S2.3 in Supporting Information S1).

3.3. Impact of InSAR Imaging Geometry

The uncertainty in the Euler vector depends on how well the measurement aperture spans the local rotational component of the velocity gradient tensor. The trade-off between the distance between the sites and the pole and the angular velocity creates an elongation of the error ellipse of the Euler pole along this radial direction (e.g., d'Alessio et al., 2005; Elliott et al., 2010). For example, 15 GNSS sites selected from Viltres et al. (2022) (Text S1 in Supporting Information S1) in northwest Arabia yield a Euler pole with high uncertainty normal to the plate motion (GNSS (NW) in Figure 4). Joint inversion with collocated InSAR velocities over northwest Arabia reduces the trade-off by a factor of two (GNSS (NW) +5InSAR in Figure 4). However, further including the InSAR data in Yemen and Oman only improves the estimate marginally, presumably due to the poor data quality in those regions (Text S2 in Supporting Information S1).

We further evaluate the effects of imaging geometry through synthetic scenarios with varying data availability: GNSS-only, InSAR LOS, or InSAR LOS combined with along-track velocity constraints (e.g., pixel tracking (Fialko et al., 2001) or burst-overlap interferometry (Grandin et al., 2016)). We use the Euler vector from Altamimi et al. (2017) to predict horizontal and LOS velocities as the synthetic inputs for SAR and GNSS

Figure 2. Time-series corrections applied to track A087 in northwest Arabia. Velocities are relative to the reference point (black square) near the global navigation satellite system site HALY. Positive velocities move toward the satellite. The L2-norm of the best-fit linear ramp coefficients to the velocity field (Text S2.2 in Supporting Information S1) is shown in the upper right of each panel. (a–e) Apparent LOS velocities of each correction term (note varying color scale ranges). (a) The ionospheric delay estimated from December 2014 to February 2023. (b) Same as (a), but only considering data until January 2022. (f–h) The original velocity in ITRF, after corrections in ITRF2014, and after corrections in the Arabia-fixed frame. The total electron content unit shows annual and 11-year fluctuations of the ionosphere (Noll, 2010). (i) Time series averaged over the black rectangle at the southeast of panels (a and b) The dashed lines indicate the best-fit apparent velocity depending on the time period being considered. σ_x denotes the temporal standard deviation. (j) L2-norms of the linear ramp coefficients in all epochs. (k) Standard deviations of the displacement fields in all epochs. $\tilde{x}$ indicates the temporal average for each quantity.

10.1029/2025GL115137

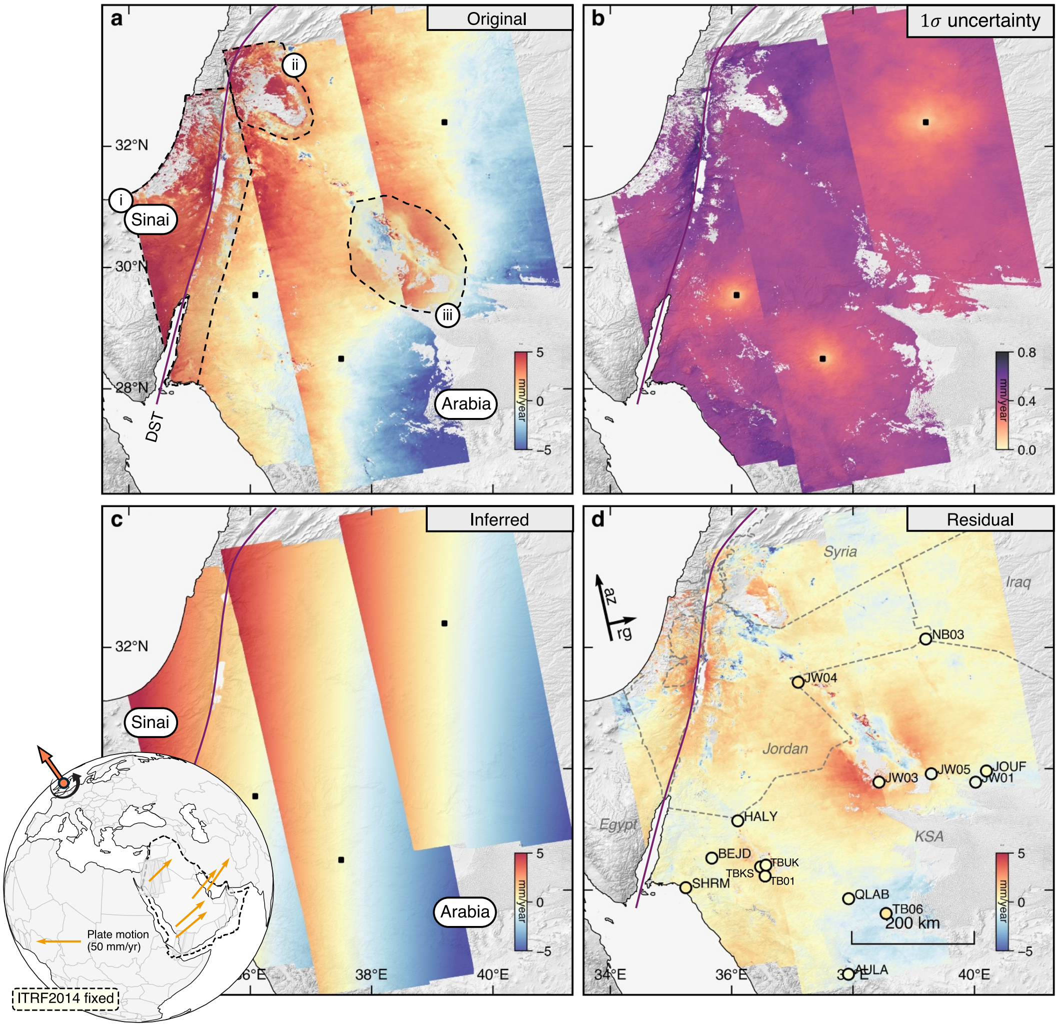

Figure 3. Three overlapping ascending tracks of velocity in northwest Arabia showing the consistent impact of Arabian motion in ITRF2014. (a) Observed line-of-sight (LOS) velocities referenced to the black squares in each of the respective tracks. We masked out areas (i) near and west of the Dead Sea Transform Fault, (ii) a large decorrelated area, and (iii) areas with >100 km wide uplift in Wadi Sirhan Basin. (b) The 1-σ uncertainties of velocities, that is, the diagonals of $\mathbf{C}_{d_t}^{0.5}$. (c) Inferred Arabian rotation. (d) Arabian-fixed LOS velocities after removing the inferred rotation from (a). Circles: global navigation satellite system horizontal velocities projected into the radar LOS, with the same color coding as Interferometric Synthetic Aperture Radar (InSAR) velocity. Inset globe: the inferred Euler pole from all nine InSAR tracks and the modeled horizontal motions at the five stations used in defining the Arabian Euler vector in ITRF2014 (Altamimi et al., 2017).

inversions, respectively. For tests including SAR synthetics, we assume measurement errors $\mathbf{C}_{d_t}$ as referenced in Figure 3a and neglect $\mathbf{C}_p$. For the GNSS-only synthetics, we adopt the measurement errors of Viltres et al. (2022). In each case, we compute (a) the Euler vector, $\hat{\mathbf{m}}$ and its covariance matrix, $\mathbf{C}_{\hat{m}}$, (b) the system's condition number, (c) the angular velocity difference from the input, $\|\hat{\mathbf{m}} - \mathbf{m}_{\text{Altamimi et al., 2017}}\|$ (°/Ma), and (d) the post-fit residual RMS (Figure 5).

The best solution is achieved using the full GNSS network (gnss). Using 20 stations spanning the breadth of the plate (gnssEW) reaches a similar result. However, when using only 15 stations from northwest Arabia (gnssNW), the yielded Euler vector has high trade-off. For InSAR scenarios, using exclusively ascending or descending geometries results in significant bias in the pole location and large $\mathbf{C}_{\hat{m}}$. For example, the 1A (one Ascending track), 1D (one Descending), and 2A (two Ascending) cases ($|\Delta D| > 708.9$ km) are ill-conditioned and prone to over-fitting (low post-fit RMS), exhibiting spurious north-south motion (Figure 5 and the labels defined therein).

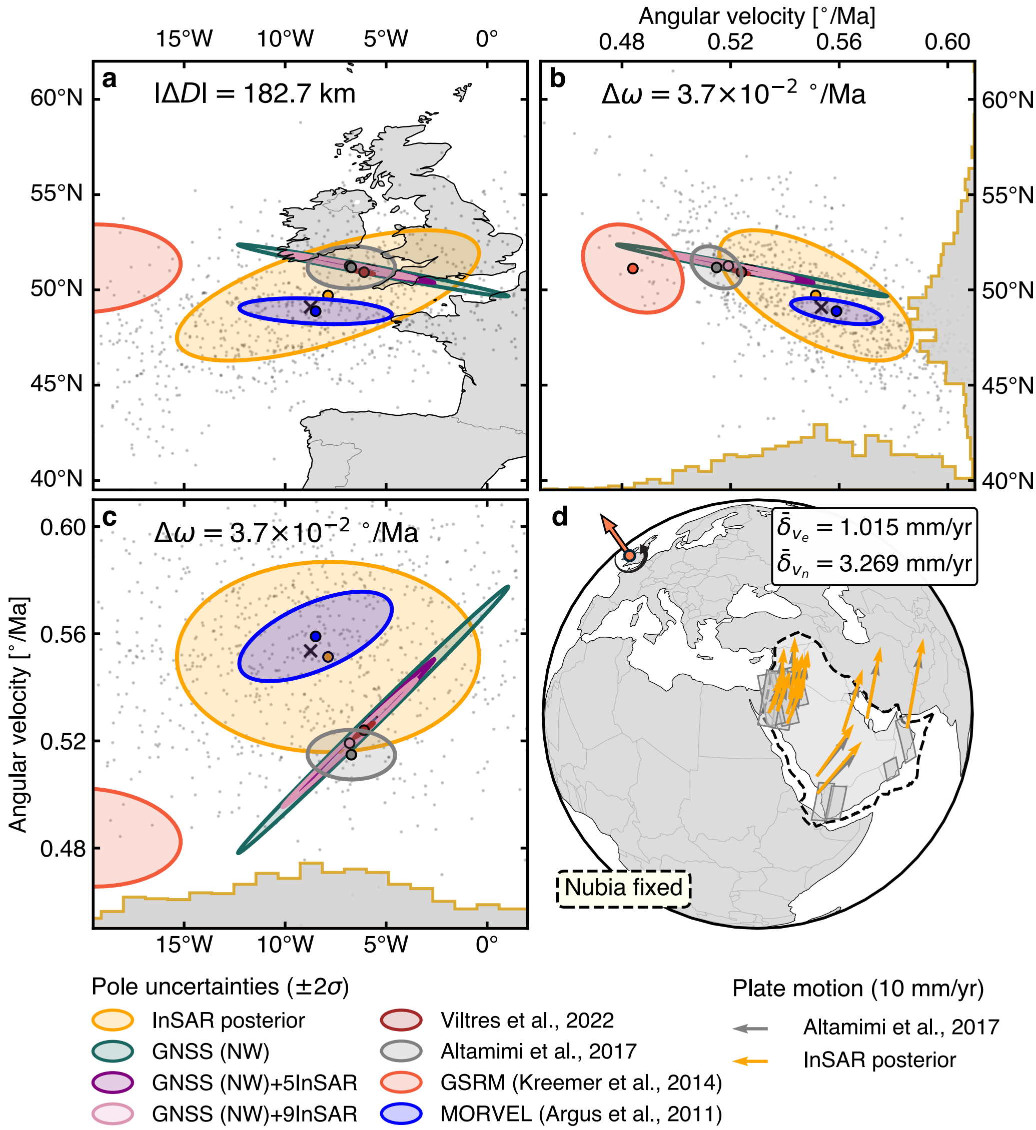

Figure 4. (a–c) Arabian plate Euler vectors (defined in ITRF2014) and uncertainties. The "x" marker shows the vector derived from velocities in Figure 3a. Scattered gray points represent the ensemble of Euler vectors estimated using different reference pixels, with marginal distributions plotted as histograms. The orange ellipse marks the final posterior vector. GNSS (NW) is based on 15 global navigation satellite system (GNSS) stations in northwest Arabia (Viltres et al., 2022), GNSS (NW) +5InSAR is the joint inversion with five Interferometric Synthetic Aperture Radar (InSAR) tracks in NW Arabia, and GNSS(NW) +9InSAR is a joint inversion including all InSAR data sets. $|\Delta D|$ and $\Delta\omega$ are the distance and rotation rate differences between our InSAR-derived vector and Altamimi et al. (2017). (d) Predicted horizontal velocities (in stable Nubia) of the InSAR-only posterior vector evaluated at GNSS sites. The mean differences in east $(\bar{\delta}_{v_e})$ and north $(\bar{\delta}_{v_n})$ components are compared with Altamimi et al. (2017).

Two or more LOS geometries are needed to constrain an Euler vector with a reasonable 2-sigma bound that overlaps the benchmark.

Due to the near-polar orbit and consistent right-looking geometry of conventional satellites like Sentinel-1, the sensitivity to the north-south displacement field is limited (e.g., Brouwer & Hanssen, 2023). The null space associated with the limited diversity of imaging geometry absorbs non-rotational long-wavelength signals in the LOS measurements by inflating the apparent north-south motion. Residual noise of at mm/yr level both at the reference pixel and in long wavelengths can elongate the error ellipse of the derived Euler vector along N60°E (Figure 4a). As a result, while synthetic scenarios 3A (three Ascending), 4AD (two Ascending and two Descending), etc., constrain the Euler vector within the 2-sigma bounds of the solution from Altamimi

10.1029/2025GL115137

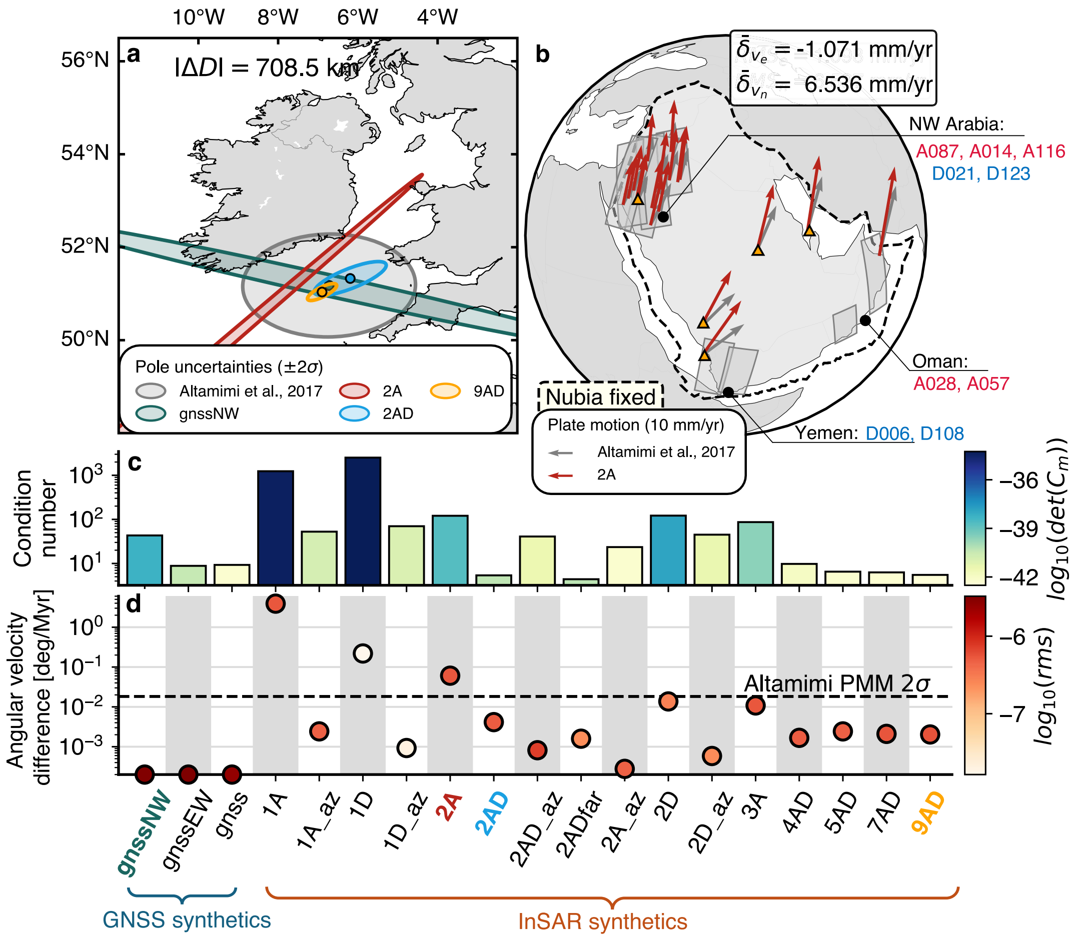

Figure 5. Synthetic scenarios with various sensing geometries. (a) Same style as Figure 4a. $|\Delta D|$ denotes the distance of 2A from Altamimi et al. (2017). (b) Same style as Figure 4d. (c) Model sensitivity: the condition number of **G** and the determinant of $\mathbf{C}_{\hat{\mathrm{m}}}$. (d) Angular velocity difference from Altamimi et al. (2017) in Cartesian space. Dots are colored by residual RMS. Labeling for global navigation satellite system (GNSS)-only synthetics: gnssNW denotes 15 stations in NW Arabia; gnssEW denotes 20 sparse GNSS sites in panel (b). gnss denotes the full GNSS network in Arabia (Figure 1). Labeling for Interferometric Synthetic Aperture Radar (InSAR) synthetics: the numeric denotes the total number of track(s), "A" denotes ascending data, and "D" for descending data. 1A: one ascending track, A087. 1D: one descending track, D021. 2A: two ascending tracks, A087 and A014. 2ADfar: one ascending in NW Arabia and one descending in Oman, A057 and D021. 2D: D021 and D123. 2AD: A087 and A014. 3A: A087, A014, and A116. 4AD: 3A and D021. 5AD: five tracks in northwest Arabia. 7AD: seven tracks in northwest Arabia and Oman 9AD: all InSAR tracks. The subscript "az" indicates inclusion of the synthetic azimuthal velocity.

et al. (2017), our observations do not. Incorporating azimuthal displacements or future left-looking measurements could improve the solution (e.g., Rosen & Kumar, 2021; Wright et al., 2004).

3.4. Referencing Multi-Track InSAR Velocities

Multi-track InSAR velocities are typically stitched to form a regional-scale deformation field by empirically aligning each track or frame to collocated GNSS (e.g., Lemrabet et al., 2023; Ou et al., 2022; Weiss et al., 2020; Xu et al., 2021). However, this data-driven approach ties InSAR long-wavelength components to GNSS, and requires a well-distributed GNSS network. By inferring and removing the Arabian block rotation, we isolate intra-plate deformation from the observed velocities, thus providing a potentially more independent approach for referencing multi-track InSAR velocities.

Our Arabia-fixed velocities are consistent across multiple tracks and with GNSS LOS velocities (Viltres et al., 2022) without empirical adjustments (Figure 3d and Figure S12 in Supporting Information S1). The consistency suggests that (a) the overlapping tracks do not experience significant relative intra-plate deformation nor vertical motion; (b) the relative horizontal and vertical motion between the reference pixels are negligible; (c) the effect of residual tropospheric noise on velocities sampled at different days by radar satellites are negligible. Thus, we infer that the velocity field primarily characterize the underlying rigid Arabian plate (ArRajehi et al., 2010; Vigny et al., 2006; Viltres et al., 2022), and the post-fit residuals are localized deformation confined within areas such as Dead Sea and the Wadi Sirhan Basin. In regions where large-scale vertical or distributed deformation ($\mathbf{d}_\varepsilon$) across multiple tracks cannot be overlooked (e.g., Great Lakes and Western US), a rigid plate assumption is inappropriate and the inversion will be biased. In such cases, one must account for the impact of mean rotation in ITRF on apparent strain or reconcile with existing GNSS networks empirically.

4. Conclusions

We infer the angular velocity vector of the Arabian plate using large-scale InSAR velocity fields in ITRF14. Plate rotation, manifested as a relative velocity gradient of ~2.1 mm/yr/100 km due to varying line-of-sight sensitivity, is extracted after mitigating long-wavelength path delays. Ionospheric effects emerge as the dominant nuisance origin, contributing to 0.8–2.0 mm/yr/100 km of apparent gradient in C-band velocity fields, an order of magnitude larger than tropospheric and tidal signals. The InSAR-derived Euler vector agrees with GNSS-based results and exhibits mean differences of 1.0 (east) and 3.3 (north) mm/yr. A persistent bias in the InSAR-based solution arises from poor north-south sensitivity coupled with unaccounted-for long-wavelength noise. This work demonstrates the methodology to assess reference frame effects in InSAR velocity fields and to integrate them with conventional ground networks for high-resolution plate kinematic models. However, caution is warranted when extending this approach to regions with significant large-scale vertical motion and intra-plate distributed deformation.

Data Availability Statement

Copernicus Sentinel-1 SLCs are provided by the European Space Agency, accessed from ASF DAAC (2020/2023) via Seamless SAR Archive (SSARA, 2023). Interferograms are processed with `stackSentinel` (Fattahi et al., 2017) in the InSAR Scientific Computing Environment (Rosen et al., 2012). Time-series analysis is performed using `MintPy` (Yunjun et al., 2019). The ocean tidal loading correction is based on global ocean tidal model `TPXO09 Atlas` (Egbert & Erofeeva, 2002). Our plate motion modeling codes are available on Liu (2025). The time-series and velocity data are available on Liu et al. (2025). Figures were made with Matplotlib (Hunter, 2007), Cartopy (Met Office, 2010/2015), and Geopandas (Jordahl et al., 2020).

Acknowledgments

We appreciate the constructive feedback from reviewers Jeff Freymueller and Marie-Pierre Doin. Thanks to Cunren Liang, Rishav Mallick, Yujie Zheng, Lijun Zhu, Leonid Pereiaslov, Shaozhou Liu, and Joann Stock for fruitful discussions. This work was partially supported by NASA Grant 80NSSC22K1910 as well as from the King Abdulaziz City for Science and Technology program for work carried out at the California Institute of Technology.

References

Agram, P. S., & Simons, M. (2015). A noise model for InSAR time series. *Journal of Geophysical Research: Solid Earth*, *120*(4), 2752–2771. https://doi.org/10.1002/2014JB011271

Altamimi, Z., Métivier, L., Rebischung, P., Rouby, H., & Collilieux, X. (2017). ITRF2014 plate motion model. *Geophysical Journal International*, *209*(3), 1906–1912. https://doi.org/10.1093/gji/ggx136

Argus, D. F., & Gordon, R. G. (1996). Tests of the rigid-plate hypothesis and bounds on intraplate deformation using geodetic data from very long baseline interferometry. *Journal of Geophysical Research*, *101*(B6), 13555–13572. https://doi.org/10.1029/95JB03775

Argus, D. F., Gordon, R. G., & DeMets, C. (2011). Geologically current motion of 56 plates relative to the no-net-rotation reference frame. *Geochemistry, Geophysics, Geosystems*, *12*(11). https://doi.org/10.1029/2011GC003751

ArRajehi, A., McClusky, S., Reilinger, R., Daoud, M., Alchalbi, A., Ergintav, S., et al. (2010). Geodetic constraints on present-day motion of the Arabian plate: Implications for Red Sea and Gulf of Aden rifting. *Tectonics*, *29*(3). https://doi.org/10.1029/2009TC002482

ASF DAAC. (2020/2023). Alaska satellite facility DAAC. Retrieved from https://asf.alaska.edu/asf/asf-services-data-discovery/

Bähr, H. (2013). Orbital effects in spaceborne synthetic aperture radar interferometry. *Dissertation (external)*. https://doi.org/10.5445/KSP/1000037166

Bähr, H., Samiei-Esfahany, S., & Hanssen, R. F. (2012). *On the effect of reference frame motion on InSAR deformation estimates. In fringe 2011* (Vol. 697). Proc. Fringe 2011. Retrieved from https://ui.adsabs.harvard.edu/abs/2012ESASP.697E..29B.29.

Berardino, P., Fornaro, G., Lanari, R., & Sansosti, E. (2002). A new algorithm for surface deformation monitoring based on small baseline differential SAR interferograms. *IEEE Transactions on Geoscience and Remote Sensing*, *40*(11), 2375–2383. https://doi.org/10.1109/TGRS.2002.803792

Biggs, J., Wright, T., Lu, Z., & Parsons, B. (2007). Multi-interferogram method for measuring interseismic deformation: Denali Fault, Alaska. *Geophysical Journal International*, *170*(3), 1165–1179. https://doi.org/10.1111/j.1365-246X.2007.03415.x

Bird, P. (2003). An updated digital model of plate boundaries. *Geochemistry, Geophysics, Geosystems*, *4*(3). https://doi.org/10.1029/2001GC000252

Bletery, Q., Cavalié, O., Nocquet, J.-M., & Ragon, T. (2020). Distribution of interseismic coupling along the North and East Anatolian faults inferred from InSAR and GPS data. *Geophysical Research Letters*, *47*(16), e2020GL087775. https://doi.org/10.1029/2020GL087775

Brouwer, W. S., & Hanssen, R. F. (2023). A treatise on InSAR geometry and 3-D displacement estimation. *IEEE Transactions on Geoscience and Remote Sensing*, *61*, 1–11. https://doi.org/10.1109/TGRS.2023.3322595

10.1029/2025GL115137

Cao, Y., Jónsson, S., & Li, Z. (2021). Advanced InSAR tropospheric corrections from global atmospheric models that incorporate spatial stochastic properties of the troposphere. *Journal of Geophysical Research: Solid Earth*, *126*(5), e2020JB020952. https://doi.org/10.1029/2020JB020952

Castro-Perdomo, N., Viltres, R., Masson, F., Klinger, Y., Liu, S., Dhahry, M., et al. (2021). Interseismic deformation in the Gulf of Aqaba from GPS measurements. *Geophysical Journal International*, *228*(1), 477–492. https://doi.org/10.1093/gji/ggab353

Cavalié, O., Lasserre, C., Doin, M. P., Peltzer, G., Sun, J., Xu, X., & Shen, Z. K. (2008). Measurement of interseismic strain across the Haiyuan fault (Gansu, China), by InSAR. *Earth and Planetary Science Letters*, *275*(3–4), 246–257. https://doi.org/10.1016/j.epsl.2008.07.057

Chaussard, E., Bürgmann, R., Fattahi, H., Johnson, C. W., Nadeau, R., Taira, T., & Johanson, I. (2015). Interseismic coupling and refined earthquake potential on the Hayward-Calaveras Fault zone. *Journal of Geophysical Research: Solid Earth*, *120*, 8570–8590. https://doi.org/10.1002/2015JB012230

Chaussard, E., Bürgmann, R., Fattahi, H., Nadeau, R. M., Taira, T., Johnson, C. W., & Johanson, I. (2015). Potential for larger earthquakes in the East San Francisco Bay area due to the direct connection between the Hayward and Calaveras faults. *Geophysical Research Letters*, *42*, 2734–2741. https://doi.org/10.1002/2015GL063575

Chaussard, E., Johnson, C. W., Fattahi, H., & Bürgmann, R. (2016). Potential and limits of InSAR to characterize interseismic deformation independently of GPS data: Application to the Southern San Andreas Fault system. *Geochemistry, Geophysics, Geosystems*, *17*(3), 1214–1229. https://doi.org/10.1002/2015GC006246

Chen, C., & Zebker, H. (2002). Phase unwrapping for large SAR interferograms: Statistical segmentation and generalized network models. *IEEE Transactions on Geoscience and Remote Sensing*, *40*(8), 1709–1719. https://doi.org/10.1109/TGRS.2002.802453

Cox, A., & Hart, R. B. (1986). *Plate tectonics: How it works*. John Wiley and Sons.

d'Alessio, M. A., Johanson, I. A., Bürgmann, R., Schmidt, D. A., & Murray, M. H. (2005). Slicing up the San Francisco Bay Area: Block kinematics and fault slip rates from GPS-derived surface velocities. *Journal of Geophysical Research*, *110*(B6). https://doi.org/10.1029/2004JB003496

DeMets, C., Gordon, R. G., & Argus, D. F. (2010). Geologically current plate motions. *Geophysical Journal International*, *181*, 1–80. https://doi.org/10.1111/j.1365-246X.2009.04491.x

DiCaprio, C. J., & Simons, M. (2008). Importance of ocean tidal load corrections for differential InSAR. *Geophysical Research Letters*, *35*(22), L22309. https://doi.org/10.1029/2008GL035806

Duputel, Z., Rivera, L., Fukahata, Y., & Kanamori, H. (2012). Uncertainty estimations for seismic source inversions. *Geophysical Journal International*, *190*(2), 1243–1256. https://doi.org/10.1111/j.1365-246X.2012.05554.x

Egbert, G. D., & Erofeeva, S. Y. (2002). Efficient inverse modeling of Barotropic Ocean tides. *Journal of Atmospheric and Oceanic Technology*, *19*(2), 183–204. https://doi.org/10.1175/1520-0426(2002)019<0183:EIMOBO>2.0.CO;2

Elliott, J. L., Larsen, C. F., Freymueller, J. T., & Motyka, R. J. (2010). Tectonic block motion and glacial isostatic adjustment in Southeast Alaska and adjacent Canada constrained by GPS measurements. *Journal of Geophysical Research*, *115*(B9). https://doi.org/10.1029/2009JB007139

Emardson, T. R., Simons, M., & Webb, F. H. (2003). Neutral atmospheric delay in interferometric synthetic aperture radar applications: Statistical description and mitigation. *Journal of Geophysical Research*, *108*(B5). https://doi.org/10.1029/2002JB001781

Farr, T. G., Rosen, P. A., Caro, E., Crippen, R., Duren, R., Hensley, S., et al. (2007). The shuttle radar topography mission. *Reviews of Geophysics*, *45*(2). https://doi.org/10.1029/2005RG000183

Fattahi, H., Agram, P., & Simons, M. (2017). A network-based enhanced spectral diversity approach for TOPS time-series analysis. *IEEE Transactions on Geoscience and Remote Sensing*, *55*(2), 777–786. https://doi.org/10.1109/TGRS.2016.2614925

Fattahi, H., & Amelung, F. (2013). DEM error correction in InSAR time series. *IEEE Transactions on Geoscience and Remote Sensing*, *51*(7), 4249–4259. https://doi.org/10.1109/TGRS.2012.2227761

Fattahi, H., & Amelung, F. (2014). InSAR uncertainty due to orbital errors. *Geophysical Journal International*, *199*(1), 549–560. https://doi.org/10.1093/gji/ggu276

Fattahi, H., & Amelung, F. (2015). InSAR bias and uncertainty due to the systematic and stochastic tropospheric delay. *Journal of Geophysical Research: Solid Earth*, *120*(12), 8758–8773. https://doi.org/10.1002/2015JB012419

Fialko, Y. (2006). Interseismic strain accumulation and the earthquake potential on the Southern San Andreas Fault system. *Nature*, *441*(7096), 968–971. https://doi.org/10.1038/nature04797

Fialko, Y., Simons, M., & Agnew, D. (2001). The complete (3-D) surface displacement field in the epicentral area of the 1999 M7.1 Hector Mine Earthquake, California, from space geodetic observations. *Geophysical Research Letters*, *28*(16), 3063–3066. https://doi.org/10.1029/2001GL013174

Goldstein, R. M., & Werner, C. L. (1998). Radar interferogram filtering for geophysical applications. *Geophysical Research Letters*, *25*(21), 4035–4038. https://doi.org/10.1029/1998GL900033

Gomba, G., Parizzi, A., De Zan, F., Eineder, M., & Bamler, R. (2016). Toward operational compensation of ionospheric effects in SAR interferograms: The split-spectrum method. *IEEE Transactions on Geoscience and Remote Sensing*, *54*(3), 1446–1461. https://doi.org/10.1109/TGRS.2015.2481079

Grandin, R., Klein, E., Métois, M., & Vigny, C. (2016). Three-dimensional displacement field of the 2015 Mw8.3 Illapel earthquake (Chile) from across- and along-track Sentinel-1 TOPS interferometry. *Geophysical Research Letters*, *43*, 2552–2561. https://doi.org/10.1002/2016GL067954

Gray, A. L., Mattar, K. E., & Sofko, G. (2000). Influence of ionospheric electron density fluctuations on satellite radar interferometry. *Geophysical Research Letters*, *27*(10), 1451–1454. https://doi.org/10.1029/2000GL000016

Guarnieri, A. M., & Tebaldini, S. (2008). On the exploitation of target statistics for SAR interferometry applications. *IEEE Transactions on Geoscience and Remote Sensing*, *46*(11), 3436–3443. https://doi.org/10.1109/TGRS.2008.2001756

Hanssen, R. F. (2001). *Radar interferometry: Data interpretation and error analysis*. Springer Science and Business Media.

Hersbach, H., Bell, B., Berrisford, P., Hirahara, S., Horányi, A., Muñoz-Sabater, J., et al. (2020). The ERA5 global reanalysis. *Quarterly Journal of the Royal Meteorological Society*, *146*(730), 1999–2049. https://doi.org/10.1002/qj.3803

Hetland, E. A., Musé, P., Simons, M., Lin, Y. N., Agram, P. S., & DiCaprio, C. J. (2012). Multiscale InSAR Time Series (MInTS) analysis of surface deformation. *Journal of Geophysical Research*, *117*(B2). https://doi.org/10.1029/2011JB008731

Hunter, J. D. (2007). Matplotlib: A 2D graphics environment. *Computer Science and Engineering*, *9*(3), 90–95. https://doi.org/10.1109/MCSE.2007.55

Jolivet, R., Agram, P. S., Lin, N. Y., Simons, M., Doin, M.-P., Peltzer, G., & Li, Z. (2014). Improving InSAR geodesy using global atmospheric models. *Journal of Geophysical Research: Solid Earth*, *119*(3), 2324–2341. https://doi.org/10.1002/2013JB010588

Jolivet, R., Grandin, R., Lasserre, C., Doin, M.-P., & Peltzer, G. (2011). Systematic InSAR tropospheric phase delay corrections from global meteorological reanalysis data. *Geophysical Research Letters*, *38*(17). https://doi.org/10.1029/2011GL048757

Jolivet, R., Simons, M., Agram, P. S., Duputel, Z., & Shen, Z.-K. (2015). Aseismic slip and seismogenic coupling along the Central San Andreas Fault. *Geophysical Research Letters*, *42*(2), 297–306. https://doi.org/10.1002/2014GL062222

Jónsson, S., Zebker, H., Segall, P., & Amelung, F. (2002). Fault slip distribution of the 1999 mw 7.1 Hector Mine, California, earthquake, estimated from satellite radar and GPS measurements. *Bulletin of the Seismological Society of America*, *92*(4), 1377–1389. https://doi.org/10.1785/0120000922

Jordahl, K., Bossche, J. V. D., Fleischmann, M., Wasserman, J., McBride, J., Gerard, J., et al. (2020). *Geopandas/geopandas: V0.8.1*. https://doi.org/10.5281/zenodo.3946761

Klinger, Y., Rivera, L., Haessler, H., & Maurin, J.-C. (1999). Active faulting in the Gulf of Aqaba: New knowledge from the MW 7.3 earthquake of 22 November 1995. *Bulletin of the Seismological Society of America*, *89*(4), 1025–1036. https://doi.org/10.1785/BSSA0890041025

Kreemer, C., Blewitt, G., & Klein, E. C. (2014). A geodetic plate motion and global strain rate model. *Geochemistry, Geophysics, Geosystems*, *15*(10), 3849–3889. https://doi.org/10.1002/2014GC005407

Lazecký, M., Hooper, A. J., & Piromthong, P. (2023). InSAR-derived horizontal velocities in a global reference frame. *Geophysical Research Letters*, *50*(10), e2022GL101173. https://doi.org/10.1029/2022GL101173

Lemrabet, L., Doin, M.-P., Lasserre, C., & Durand, P. (2023). Referencing of continental-scale InSAR-derived velocity fields: Case study of the Eastern Tibetan plateau. *Journal of Geophysical Research: Solid Earth*, *128*(7), e2022JB026251. https://doi.org/10.1029/2022JB026251

Le Pichon, X., & Kreemer, C. (2010). The Miocene-to-present kinematic evolution of the eastern Mediterranean and Middle East and its implications for dynamics. *Annual Review of Earth and Planetary Sciences*, *38*(1), 323–351. https://doi.org/10.1146/annurev-earth-040809-152419

Li, X., Jónsson, S., & Cao, Y. (2021). Interseismic deformation from Sentinel-1 burst-overlap interferometry: Application to the Southern Dead Sea Fault. *Geophysical Research Letters*, *48*(16), e2021GL093481. https://doi.org/10.1029/2021GL093481

Liang, C., Agram, P., Simons, M., & Fielding, E. J. (2019). Ionospheric correction of InSAR time series analysis of C-band Sentinel-1 TOPS data. *IEEE Transactions on Geoscience and Remote Sensing*, *57*(9), 6755–6773. https://doi.org/10.1109/TGRS.2019.2908494

Liu, Y.-K. (2025). PyPMM: Initial release (v0) [software]. *GitHub*. https://github.com/yuankailiu/PyPMM/tree/Initial-release

Liu, Y.-K., Yunjun, Z., & Simons, M. (2025). InSAR time series and velocities in northwest Arabia, Yemen, and Oman (1.0) [Dataset]. *Zenodo*. https://zenodo.org/records/15361124

Lohman, R. B., & Simons, M. (2005). Some thoughts on the use of InSAR data to constrain models of surface deformation: Noise structure and data downsampling. *Geochemistry, Geophysics, Geosystems*, *6*(1). https://doi.org/10.1029/2004GC000841

Loveless, J. P., & Meade, B. J. (2010). Geodetic imaging of plate motions, slip rates, and partitioning of deformation in Japan. *Journal of Geophysical Research*, *115*(B2). https://doi.org/10.1029/2008JB006248

Mahmoud, S., Reilinger, R., McClusky, S., Vernant, P., & Tealeb, A. (2005). GPS evidence for northward motion of the Sinai Block: Implications for E. Mediterranean tectonics. *Earth and Planetary Science Letters*, *238*(1–2), 217–224. https://doi.org/10.1016/j.epsl.2005.06.063

Martens, H. R., Rivera, L., & Simons, M. (2019). LoadDef: A python-based toolkit to model elastic deformation caused by surface mass loading on spherically symmetric bodies. *Earth and Space Science*, *6*(2), 311–323. https://doi.org/10.1029/2018EA000462

Massonnet, D., & Feigl, K. L. (1998). Radar interferometry and its application to changes in the Earth's surface. *Reviews of Geophysics*, *36*(4), 441–500. https://doi.org/10.1029/97RG03139

Massonnet, D., Rossi, M., Carmona, C., Adragna, F., Peltzer, G., Feigl, K., & Rabaute, T. (1993). The displacement field of the Landers earthquake mapped by radar interferometry. *Nature*, *364*(6433), 138–142. https://doi.org/10.1038/364138a0

McCaffrey, R. (2005). Block kinematics of the Pacific–North America plate boundary in the southwestern United States from inversion of GPS, seismological, and geologic data. *Journal of Geophysical Research*, *110*(B7). https://doi.org/10.1029/2004JB003307

McKenzie, D. P., & Parker, R. L. (1967). The North Pacific: An example of tectonics on a sphere. *Nature*, *216*(5122), 1276–1280. https://doi.org/10.1038/2161276a0

Meade, B. J., & Loveless, J. P. (2009). Block modeling with connected fault-network geometries and a linear elastic coupling estimator in spherical coordinates. *Bulletin of the Seismological Society of America*, *99*(6), 3124–3139. https://doi.org/10.1785/0120090088

Met Office. (2010/2015). Cartopy: A cartographic python library with a Matplotlib interface. Retrieved from https://scitools.org.uk/cartopy

Meyer, F. (2010). A review of ionospheric effects in low-frequency SAR — Signals, correction methods, and performance requirements. in 2010. *IEEE International Geoscience and Remote Sensing Symposium*, 29–32. https://doi.org/10.1109/IGARSS.2010.5654258

Milbert, D. (2018). Solid earth tide. https://geodesyworld.github.io/SOFTS/solid.htm

Morgan, W. J. (1968). Rises, trenches, great faults, and crustal blocks. *Journal of Geophysical Research*, *1896–1977*(73), 1959–1982. https://doi.org/10.1029/JB073i006p01959

Neely, W. R., Borsa, A. A., & Silverii, F. (2020). GInSAR: A cGPS correction for enhanced InSAR time series. *IEEE Transactions on Geoscience and Remote Sensing*, *58*(1), 136–146. https://doi.org/10.1109/TGRS.2019.2934118

Noll, C. E. (2010). The crustal dynamics data information system: A resource to support scientific analysis using space geodesy. *Advances in Space Research*, *45*(12), 1421–1440. https://doi.org/10.1016/j.asr.2010.01.018

Onn, F., & Zebker, H. A. (2006). Correction for interferometric synthetic aperture radar atmospheric phase artifacts using time series of zenith wet delay observations from a GPS network. *Journal of Geophysical Research*, *111*(B9). https://doi.org/10.1029/2005JB004012

Ou, Q., Daout, S., Weiss, J. R., Shen, L., Lazecký, M., Wright, T. J., & Parsons, B. E. (2022). Large-scale interseismic strain mapping of the NE Tibetan Plateau from Sentinel-1 interferometry. *Journal of Geophysical Research: Solid Earth*, *127*(6), e2022JB024176. https://doi.org/10.1029/2022JB024176

Parizzi, A., Brcic, R., & De Zan, F. (2021). InSAR performance for large-scale deformation measurement. *IEEE Transactions on Geoscience and Remote Sensing*, *59*(10), 8510–8520. https://doi.org/10.1109/TGRS.2020.3039006

Peter, H. (2021). *Copernicus sentinel-1, -2 and -3 precise orbit determination service (CPOD)*. European Space Agency (ESA). Retrieved from https://sentinel.esa.int/documents/247904/4599719/Copernicus-POD-Product-Handbook.pdf

Pritchard, M. E., & Simons, M. (2006). An aseismic slip pulse in northern Chile and along-strike variations in seismogenic behavior. *Journal of Geophysical Research*, *111*(B8). https://doi.org/10.1029/2006JB004258

Reilinger, R., McClusky, S., Vernant, P., Lawrence, S., Ergintav, S., Cakmak, R., et al. (2006). GPS constraints on continental deformation in the Africa-Arabia-Eurasia continental collision zone and implications for the dynamics of plate interactions. *Journal of Geophysical Research*, *111*(B5). https://doi.org/10.1029/2005JB004051

Rosen, P. A., Gurrola, E., Sacco, G. F., & Zebker, H. (2012). The InSAR scientific computing environment. In *EUSAR 2012 9th Eur. Conf. Synth. Aperture radar* (pp. 730–733). Retrieved from https://ieeexplore.ieee.org/abstract/document/6217174

Rosen, P. A., & Kumar, R. (2021). NASA-ISRO SAR (NISAR) mission status. In *2021 IEEE radar Conf. RadarConf21* (pp. 1–6). https://doi.org/10.1109/RadarConf2147009.2021.9455211

Ryder, I., Parsons, B., Wright, T. J., & Funning, G. J. (2007). Post-seismic motion following the 1997 Manyi (Tibet) earthquake: InSAR observations and modelling. *Geophysical Journal International*, *169*(3), 1009–1027. https://doi.org/10.1111/j.1365-246X.2006.03312.x

Simons, M., Fialko, Y., & Rivera, L. (2002). Coseismic deformation from the 1999 mw 7.1 Hector Mine, California, earthquake as inferred from InSAR and GPS observations. *Bulletin of the Seismological Society of America*, *92*(4), 1390–1402. https://doi.org/10.1785/0120000933

SSARA. (2023). Seamless SAR archive (SSARA), EarthScope consortium. Retrieved from https://web-services.unavco.org/brokered/ssara/

Stephenson, O. L., Liu, Y.-K., Yunjun, Z., Simons, M., Rosen, P., & Xu, X. (2022). The impact of plate motions on long-wavelength InSAR-derived velocity fields. *Geophysical Research Letters*, *49*(21), e2022GL099835. https://doi.org/10.1029/2022GL099835

Tarayre, H., & Massonnet, D. (1996). Atmospheric Propagation heterogeneities revealed by ERS-1 interferometry. *Geophysical Research Letters*, *23*(9), 989–992. https://doi.org/10.1029/96GL00622

Tong, X., Sandwell, D. T., & Smith-Konter, B. (2013). High-resolution interseismic velocity data along the San Andreas Fault from GPS and InSAR. *Journal of Geophysical Research: Solid Earth*, *118*, 369–389. https://doi.org/10.1029/2012JB009442

Tong, X., Smith-Konter, B., & Sandwell, D. T. (2014). Is there a discrepancy between geological and geodetic slip rates along the San Andreas Fault System? *Journal of Geophysical Research: Solid Earth*, *119*, 2518–2538. https://doi.org/10.1002/2013JB010765

Tough, J. A., Blacknell, D., & Quegan, S. (1995). A statistical description of polarimetric and interferometric synthetic aperture radar data. *Proceedings of the Royal Society of London. Series A*, *449*, 567–589. https://doi.org/10.1098/rspa.1995.0059

Vasyura-Bathke, H., Dettmer, J., Dutta, R., Mai, P. M., & Jónsson, S. (2021). Accounting for theory errors with empirical Bayesian noise models in nonlinear centroid moment tensor estimation. *Geophysical Journal International*, *225*(2), 1412–1431. https://doi.org/10.1093/gji/ggab034

Vigny, C., Huchon, P., Ruegg, J.-C., Khanbari, K., & Asfaw, L. M. (2006). Confirmation of Arabia plate slow motion by new GPS data in Yemen. *Journal of Geophysical Research*, *111*(B2). https://doi.org/10.1029/2004JB003229

Viltres, R., Jónsson, S., Alothman, A., Liu, S., Leroy, S., Masson, F., et al. (2022). Present-day motion of the Arabian plate. *Tectonics*, *41*(3), e2021TC007013. https://doi.org/10.1029/2021TC007013

Weiss, J. R., Walters, R. J., Morishita, Y., Wright, T. J., Lazecky, M., Wang, H., et al. (2020). High-resolution surface velocities and strain for Anatolia from sentinel-1 InSAR and GNSS data. *Geophysical Research Letters*, *47*(17), e2020GL087376. https://doi.org/10.1029/2020GL087376

Wright, T. J., Parsons, B. E., & Lu, Z. (2004). Toward mapping surface deformation in three dimensions using InSAR. *Geophysical Research Letters*, *31*(1). https://doi.org/10.1029/2003GL018827

Xu, X., & Sandwell, D. T. (2020). Toward absolute phase change recovery with InSAR: Correcting for earth tides and phase unwrapping ambiguities. *IEEE Transactions on Geoscience and Remote Sensing*, *58*(1), 726–733. https://doi.org/10.1109/TGRS.2019.2940207

Xu, X., Sandwell, D. T., Klein, E., & Bock, Y. (2021). Integrated sentinel-1 InSAR and GNSS time-series along the San Andreas Fault system. *Journal of Geophysical Research: Solid Earth*, *126*(11), e2021JB022579. https://doi.org/10.1029/2021JB022579

Yu, C., Penna, N. T., & Li, Z. (2017). Generation of real-time mode high-resolution water vapor fields from GPS observations. *Journal of Geophysical Research: Atmospheres*, *122*(3), 2008–2025. https://doi.org/10.1002/2016JD025753

Yunjun, Z., Fattahi, H., & Amelung, F. (2019). Small baseline InSAR time series analysis: Unwrapping error correction and noise reduction. *Computers and Geosciences*, *133*, 104331. https://doi.org/10.1016/j.cageo.2019.104331

Yunjun, Z., Fattahi, H., Pi, X., Rosen, P., Simons, M., Agram, P., & Aoki, Y. (2022). Range geolocation accuracy of C-/L-Band SAR and its implications for operational stack coregistration. *IEEE Transactions on Geoscience and Remote Sensing*, *60*, 1–19. https://doi.org/10.1109/TGRS.2022.3168509

Zhang, B., Hestir, E., Yunjun, Z., Reiter, M. E., Viers, J. H., Schaffer-Smith, D., et al. (2024). Automated reference points selection for InSAR time series analysis on segmented wetlands. *IEEE Geoscience and Remote Sensing Letters*, *21*, 1–5. https://doi.org/10.1109/LGRS.2024.3390568

Zheng, Y., Fattahi, H., Agram, P., Simons, M., & Rosen, P. (2022). On closure phase and systematic bias in multilooked SAR interferometry. *IEEE Transactions on Geoscience and Remote Sensing*, *60*, 1–11. https://doi.org/10.1109/TGRS.2022.3167648

References From the Supporting Information

Bowring, B. R. (1976). Transformation from spatial to geographical coordinates. *Survey Review*, *23*(181), 323–327. https://doi.org/10.1179/sre.1976.23.181.323

Gomba, G., Rodríguez González, F., & De Zan, F. (2017). Ionospheric phase screen compensation for the sentinel-1 TOPS and ALOS-2 ScanSAR modes. *IEEE Transactions on Geoscience and Remote Sensing*, *55*, 223–235. https://doi.org/10.1109/TGRS.2016.2604461

Goudarzi, M. A., Cocard, M., & Santerre, R. (2014). Epc: Matlab software to estimate Euler pole parameters. *GPS Solutions*, *18*(1), 153–162. https://doi.org/10.1007/s10291-013-0354-4

Oliver-Cabrera, T., Jones, C. E., Yunjun, Z., & Simard, M. (2022). InSAR phase unwrapping error correction for rapid repeat measurements of water level change in wetlands. *IEEE Transactions on Geoscience and Remote Sensing*, *60*, 1–15. https://doi.org/10.1109/TGRS.2021.3108751

Sanz Subirana, J., Juan Zornoza, J., & Hernández-Pajares, M. (2011a). Ellipsoidal and cartesian coordinates conversion - Navipedia. https://gssc.esa.int/navipedia/index.php/Ellipsoidal_and_Cartesian_Coordinates_Conversion

Sanz Subirana, J., Juan Zornoza, J., & Hernández-Pajares, M. (2011b). Transformations between ECEF and ENU coordinates - Navipedia. https://gssc.esa.int/navipedia/index.php/Transformations_between_ECEF_and_ENU_coordinates